I-1.   PROJECT RESEARCHES

Project 5

PR5 Development on Neutron Imaging Application

Y. Saito

Institute for Integrated Radiation and Nuclear Science, Kyoto University

1. Objectives and Allotted Research Subjects: Neutron imaging provides valuable information which cannot be obtained from an optical or X-ray imaging. The purpose of this project is to develop the imaging method itself and also the experimental environment for expanding the application area of the neutron imaging. The allotted research subjects are as follows:

ARS-1: Measurements of Multiphase Flow Dynamics using Neutron Radiography (Y. Saito et al.)

ARS-2: Evaluation of Water Distribution and Electrochemical Characteristics in Polymer Electrolyte Fuel Cell (H. Asano et al.)

ARS-3: Neutron Radiography on the Mixing Behavior of Reaction Solution and Cooling (S. Takami et al.)

ARS-4: Visualization of Dynamic Flow Maldistribution in a Microchannel Heat Exchanger (H. Umekawa et al.)

ARS-5: Measurement of Frost Distribution by Using X-ray and Neutron Cooperative Imaging (R. Matsumoto et al.)

ARS-6: Introduction of contrast agent for X-ray-based visualization of roots planted on organic medium (U. Matsushima)

ARS-7: Effect of the water content of high-strength concrete on the spalling phenomenon under fire (M. Kanematsu et al.)

ARS-8: Visualization of Excimer cluster tracers by using Neutrons (Y. Tsuji et al.)

ARS-9: Dynamic Visualization of Hydrogen Accumulation Behavior in Metallic Materials via Neutron Imaging (K. Shimizu et al.)

ARS-10: In-situ Lithium diffusion behavior in NASICON-Type Structured Lithium Ion Conductive Composite by Means of Neutron Radiography (S. Takai et al.)

ARS-11 Visualization in the Accumulated Curved Rod Arrays (M. Kaneda)

2. Main results and the contents of this report: To develop neutron imaging, our imaging system was developed so that high-speed imaging could be per-formed at thermal neutron flux of 10^7 n/cm^{2}s. Such improved system was shared with all of the project members and valuable results were obtained as follows:

ARS-1 improved the above-mentioned high-speed imaging system at the B4 port. In this study, 1-D total variation denoising was ap-plied to image sequences measured by using a system with a high-speed camera and an image intensifier. Such denoising was applied to detect a falling sphere in the air. By applying the 1-D denoising with a parameter $\lambda = 500$, only the noise can be removed.

In addition, a neutron CT system was tested in the E-2 port. In the CT reconstruction process, TomoPy, which is an open-sourced Python toolbox. Developed system was applied to aluminum plates with holes and slits so that the CT reconstruction results could be compared to those at other neutron imaging facilities.

ARS-2 In this study, neutron radiography and electrochemical impedance spectroscopy (EIS) were employed to clarify the relationship between the water contents and the sources of polarization loss in a PEFC. As a result, the relation between the water contents in the PEM and the ionic conductivity is discussed.

ARS-3 applied neutron imaging to the flow visualization of mixing behavior of reactant streams during hydrothermal synthesis. In the synthesis process, cooling of the reaction solution may affect the particle size. In this study, temperature distribution was measured by changing the flow rate of the cooling water. From measurement results, it was confirmed that faster cooling resulted in the production of smaller nanorods.

ARS-4 applied the neutron imaging to visualization of dynamic maldistribution in a microchannel heat exchanger under non-uniformly heated conditions. The effect of heat flux distributions on the maldistribution of liquids was estimated.

ARS-5 applied neutron imaging to frosting behavior in cooling heat exchange system. Simultaneous Xray and neutron imaging was performed to clarify the 3D frost deposition at the B4 port.

ARS-6 X-ray imaging is not suitable for plant root visualization because of its low sensitivity for biological samples. However, by introducing a contrast agent into the plant roots and increasing the absorption of X-rays compared to rice husk medium, roots in the rice husk medium could be observed. Therefore, this study established a method to locate roots in culture medium with high organic matter using X-ray imaging.

ARS-7 applied neutron to measurement of effect of the water content of high-strength concrete on the spalling phenomenon under fire. In this study, the effect of moisture content on the spalling phenomena of high-strength concrete was investigated by using the neutron imaging technique.

ARS-10 applied to in-situ Lithium diffusion behavior in NASICON-Type structured Lithium Ion conductive composite. From measurement results, it indicates that the material should be changed.

ARS-11 applied to measurement of coolant distribution in the curved rod arrays simulating the stator coil for the future vehicle electro devices. In this study, the coolant visualization inside the simplified stator coil structure is carried out by using the neutron radiography. The coil structure is made of aluminum and composed by layered curved rod array.

ARS-8, 9 were not performed due to the COVID19.

R3P5

PR5-1   Measurements of multiphase flow dynamics using neutron radiography

Y. Saito, D. Ito and N. Odaira

Institute for Integrated Radiation and Nuclear Science, Kyoto University

INTRODUCTION: Enhancement of the spatial and temporal resolutions in neutron radiography (NRG) is very important for multiphase flow visualization. In this work, image denoising for high-speed neutron imaging was evaluated to observe the dynamic phenomena, and the neutron computed tomography (CT) system was improved to enhance spatial resolution.

IMAGE RESTORATION FOR HIGH-SPEED IMAGING: In high-speed neutron imaging, image noise reduction is very important to understand the phenomena from the acquired images. A lot of filtering methods have been tested to improve the neutron transmission image quality so far. In this study, 1-D total variation denoising [1] was applied to image sequences measured by using a system with a high-speed camera and an image intensifier. Figure 1 shows neutron transmission images of a free-falling metallic sphere in the air. The frame rate is 2000 fps and the exposure time is 1/3000 sec. Although the motion of the sphere can be observed, the images include many noises. The result of denoising is shown in Fig. 2. The change of the grayscale at the center point of the image in Fig .1 is plotted. The original signal represents the large fluctuation. By applying the 1-D denoising with a parameter $\lambda = 500$, only the noise can be removed. However, the signal of the falling sphere is lost as increasing the denoising parameter. Thus, optimization of the parameter should be done for each measurement object.

IMPROVEMENT OF CT SYSTEM: To increase the spatial resolution in neutron CT, a fine rotation angle and sufficient statistical accuracy are required. So, it takes a long time to get a good result. In this study, our CT system was improved to optimize the CT parameter like rotation angle and exposure time in the E-2 port. The schematic diagram of the system is illustrated in Fig. 3. A CCD camera and a rotation stage are controlled by the same software, which is developed by LabVIEW (National Instruments), on a PC. In the CT reconstruction process, TomoPy [2] which is an open-sourced Python toolbox is used. This library has a lot of reconstruction algorithms, and the grid reconstruction is chosen in the present process. The example of the CT reconstruction of measured images at the E-2 port is shown in Fig. 4. The sample is aluminum circular plates with small holes and slits. The rotation angle is 0.6 degree and the exposure time is 150 sec. As a result, it takes about 13 hours for a measurement. The location and size of the small holes could be observed clearly from the reconstructed images.
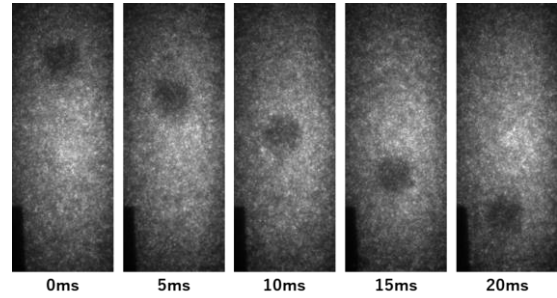

Fig. 1   Neutron transmission images of a free-falling sphere.
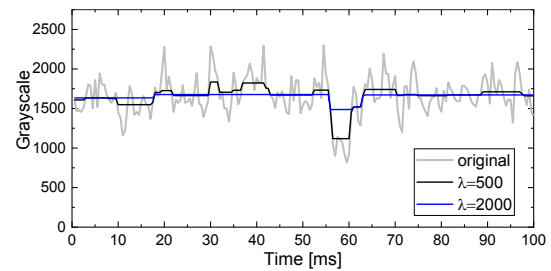

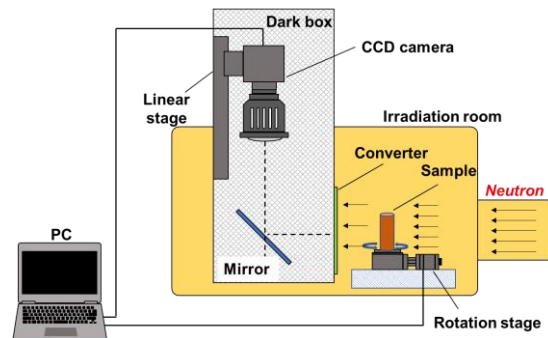Fig. 2   Time-series grayscale value of the original and denoised signals.
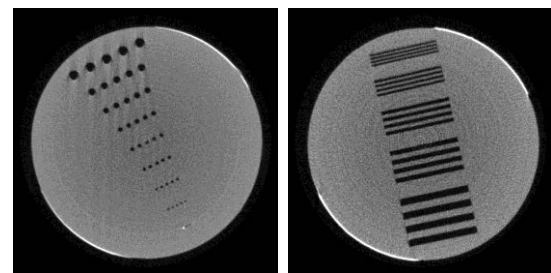

Fig. 3   Improved CT system in E-2 port.

Fig. 4   Neutron CT reconstruction results of aluminum plates with holes and slits.

REFERENCES:
[1] S.J. Kim, K. Koh, S. Boyd and D. Gorinevsky, L1 Trend Filtering, SIAM Review, **51**-2 (2009) 339-360.
[2] https://github.com/tomopy/tomopy

R3P5-1

PR5-2   Evaluation of Water Distribution and Electrochemical Characteristics in Polymer Electrolyte Fuel Cell

H. Murakawa, K. Mine, K. Mizushima, K. Sugimoto, H. Asano, D. Ito[1] and Y. Saito[1]

Graduate School of Engineering, Kobe University
[1]Institute for Integrated Radiation and Nuclear Science, Kyoto University

INTRODUCTION: Water management is a key topic of a polymer electrolyte fuel cell (PEFC). It is well known that the water accumulation in the gas diffusion layer (GDL) increases the polarization resistance, whereas the increase in the water content in the proton exchange membrane (PEM) decreases the proton conductivity in the PEM. The water distribution may change during the PEFC operation because of the water generation. However, the effect of water distribution and the water contents in the GDL and the membrane on the resistances has not been fully understood because of the difficulty of measuring water distributions in the PEFC. In this study, neutron radiography and electrochemical impedance spectroscopy (EIS) were employed to clarify the relationship between the water contents and the sources of polarization loss in a PEFC. As a result, the relation between the water contents in the PEM and the ionic conductivity is discussed.

EXPERIMENTS: A small size PEFC having a single-serpentine gas channel with a cross-sectional area of 1×1 mm^2 was used for measuring two-dimensional water distribution and the electrochemical characteristics. Nafion® NR-212 was used as the PEM with a thickness of approximately 90 μm having catalyst layers on both the anode and cathode sides. Two-dimensional water distributions were obtained every 60 sec during the PEFC operation using neutron radiography. The EIS measurements were simultaneously carried out with the neutron radiography for evaluating the PEM resistance and the reaction resistance. The experiments were carried out at room temperature.

RESULTS: Fig. 1(a) shows an example of the two-dimensional water distribution at a current density, *i*, of 158 mA/cm^2 with MPL in the parallel channels at 20 min after the start of the PEFC power generation. Condensation water is confirmed as indicated black color. It can be confirmed that the condensed water remains in the flow channels. The relation between the ionic conductivity, σ, and the water contents in the PEM, λ, was evaluated based on the experimental results. Since it was difficult to evaluate the absolute value of λ, the difference in water content, Δλ, was evaluated.
Fig. 1(b) shows the relationship between Δσ and Δλ obtained under various experimental conditions, *i.e.* single-serpentine or nine-parallel gas channels, and current density. It is clear that Δσ almost linearly increases with Δλ. It is thought that the ionic conductivity can be evaluated as a function of the water content in the PEM re-

gardless of the difference in the experimental conditions. Springer et al. [1] proposed a correlation between the ionic conductivity of the PEM and the water content in the PEM. In our experiment, the ionic conductivity was less affected by the water content than in Springer's model. It is thought that Springer's model cannot be applied under low λ conditions such as at the begging of the PEFC operation. Based on the experimental results, an empirical equation regarding the water content and the ionic conductivity is proposed particularly for lower λ.
Numerical analysis was carried out for predicting the cell voltage to compare with Springer's model and the empirical equation. The results are compared as shown in Fig. 2. By applying the equation to the numerical analysis, the difference in the cell voltage is large until 30 min from the PEFC operation. At the beginning of the PEFC operation, the water content in the PEM is low. Therefore, the difference in the ionic conductivity model affects the prediction of the cell voltage.
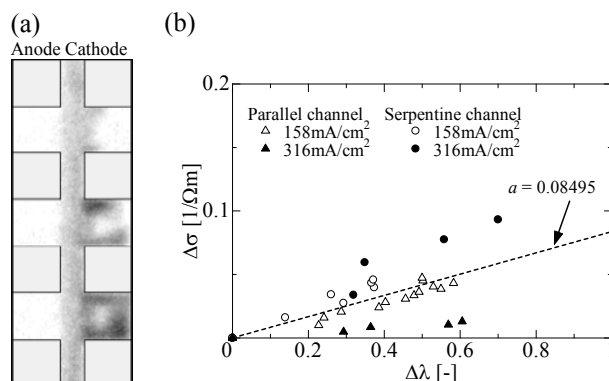

Fig. 1. Examples of the experimental results; (a) Two-dimensional water distributions obtained by neutron radiography; (b) Relation between the change of the water contents in the PEM, Δλ, and the change of the ionic conductivity, Δσ.
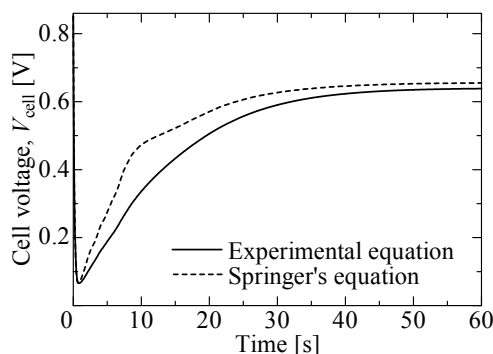

Fig. 2. Effect of the ionic conductivity models on the prediction of the cell voltage by the numerical analysis.

REFERENCES:
[1] T.E. Springer, T.A. Zawadzinski, S. Gottesfeld, J. Electrochemical Society, **138** (1991) 2334–2342.

R3P5-2

PR5-3 Neutron Radiography on the Mixing Behavior of Reaction Solution and Cooling Water at a T-shaped Junction in a Flow-type Supercritical Hydrothermal Reactor.

S. Takami, K. Sato, R. Sasaki, B. Xie, M. Kubo[1],
T. Tsukada[1], K. Sugimoto[2], N. Odaira[3], D. Ito[3], and
Y. Saito[3]

Graduate School of Engineering, Nagoya University
[1] *Graduate School of Engineering, Tohoku University*
[2] *Graduate School of Engineering, Kobe University*
[3] *Institute for Integrated Radiation and Nuclear Science, Kyoto University*

INTRODUCTION: We have synthesized metal oxide nanoparticles by mixing a stream of an aqueous reactant solution with another stream of supercritical water in a flow-type reactor. The mixed reaction solution was gradually cooled to room temperature by using a jacket cooler and released from a back pressure regulator. However, the gradual cooling might result in the production of larger nanoparticles with broader size distribution. In this study, we proposed quicker cooling of the reaction solution by mixing cooling water and observed the cooling process by neutron radiography.

EXPERIMENTS: Fig. 1 shows the schematics of the experimental apparatus. A stream of water was fed using a high-pressure pump and heated by an external heater. Simultaneously, another high-pressure pump fed a stream of room temperature water. The two streams were mixed at the mixing point to mimic the cooling process of the reaction solution by mixing. Toward this mixing point, a neutron beam was irradiated and radiography images were obtained using [6]LiF/ZnS scintillator screen.
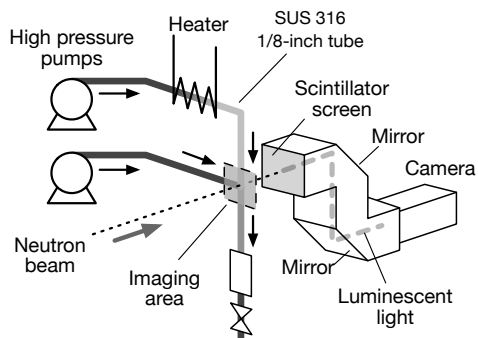

Fig. 1. Schematics of the experimental apparatus.

RESULTS: Fig. 2 shows the averaged water density in the flow channel around the T-shaped junction. The heated water (380°C, 12 g/min) was supplied from the top while the cooling water was supplied from the side (12~36 g/min). When the flow rate of the cooling water was 12 g/min, the cooling water gradually mixed with the heated water in the vertical tube. On the other hand, faster cooling was expected when the flow rate of cooling water was 24 and 36 g/min. To evaluate the change in the temperature of the heated water from the top, we evalu-

ated the density of water at the center of the vertical flow channel and estimated the temperature. Figure 3 shows the change in the temperature in the vertical tube.
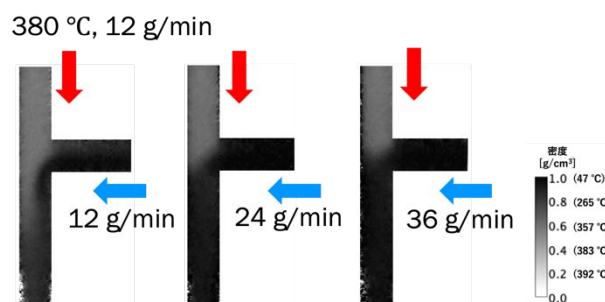

Fig. 2. Averaged water density in the flow channel. Heated water (reactant solution) and cooling water came from the top and the side, respectively.
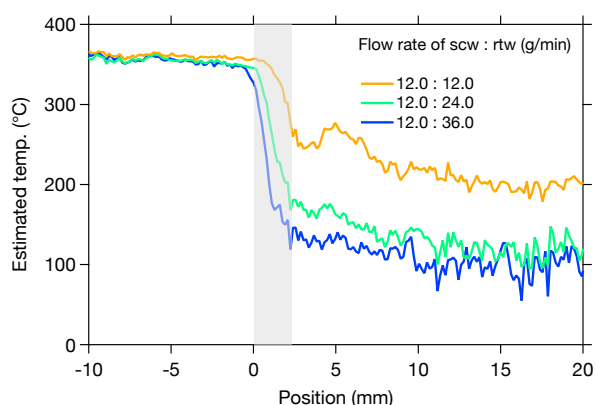

Fig. 3. Estimated temperature of the heated water in the vertical tube around the T-junction. Cooling water was mixed where the position was between 0~2.3 mm.

When the flow rate of cooling water was 24 and 36 g/min, much faster cooling was realized. We then synthesized ZnO nanorods while supplying cooling water. The results showed that nanorods with thinner diameters were obtained as we increased the rate of cooling water. These results confirmed that the size of the product by a flow-type reactor can be controlled by the rate of cooling of the reacted solution.

CONCLUSION: By performing neutron radiography measurements, we evaluated the rate of cooling of the reactant solution in the flow-type reactor and confirmed that faster cooling resulted in the production of smaller nanorods.

REFERENCES:
[1] S. Takami *et al.*, J. Supercrit. Fluids, **63** (2012) 46-51.
[2] K. Sugioka *et al.*, AIChE J., **60** (2014) 1168-1175.
[3] S. Takami *et al.,* Phys. Proc., **69** (2015) 564-569.
[4] K. Sugioka *et al.*, J. Supercrit. Fluids, **109** (2016) 43-50.

R3P5-3

PR5-4   Visualization of Dynamic Flow Maldistribution in a Microchannel Heat Exchanger

H. Umekawa[1], T. Ami[1], R. Funakura[1], K. Orido[1], K. Akiyama[1], Y. Saito[2], D. Ito[2] and N. Odaira[2]

[1]Department of Mechanical Engineering, Kansai University
[2]Institute for Integrated Radiation and Nuclear Science, Kyoto University

Fig.1 Cross section of Microchannel.

INTRODUCTION: Microchannel heat exchanger has several advantages against the conventional fin-tube heat exchanger, thus recently it has been widely used as the heat exchanger of air-conditioning unit. But the structure of microchannel fundamentally causes the flow oscillation especially under non-uniform heat flux condition.

In this series of investigation[1-3], heat and flow characteristics has been evaluated by using a single plate microchannel heat exchanger.

In this report, the quantitatively visualization of a dynamic flow maldistribution by using neutron radiography will be briefly explained.

EXPERIMENTS: The experimental apparatus is a forced convective boiling system, and the working fluid is Methanol. It has low viscosity similar with actual refrigerant (R32), and has enough attenuation coefficient for visualization. The cross section of the test-section is shown in Fig.1, and it has 9 channels with a.1.6mm diameter. The test-section is heated by Joule heating by using nichrome foils attached to the plate surface with 200 mm heating length and it can generate the nonuniform heat flux distribution. The detail construction and procedures can be shown elsewhere[1-3].

RESULTS: Figure 2(a) is a example of the time averaged visualization image under uniform heating condition. In this report, $\exp(-\mu\rho\delta)$ is used as simple image processing.

As shown in this figure, flow maldistribution can be observed visually. In the former experiment[1-3], it was difficult to evaluate the detail flow movement in each channel owing to the lack of the spacial resolution, but in this experiment which used slightly wide channel, the each channel can be clearly distinguished. Then, it can make the time strip image of each flow channel as shown in Fig.2(b). This time strip image is the stacked of time sequence images of each channel, and Fig.3 is the same data at the inlet of the visualization area is plotted against time. On the basis on these data, the propagation of wet/dry area and also correlation of flow fluctuation among each channel will be evaluated Theses characteristics will be correlated with the heat transfer characteristics.

Fig.2 Visualization image (x_{ex}=0.1- G=50kg/m²s).
(a) Time average image (b)Time strip image
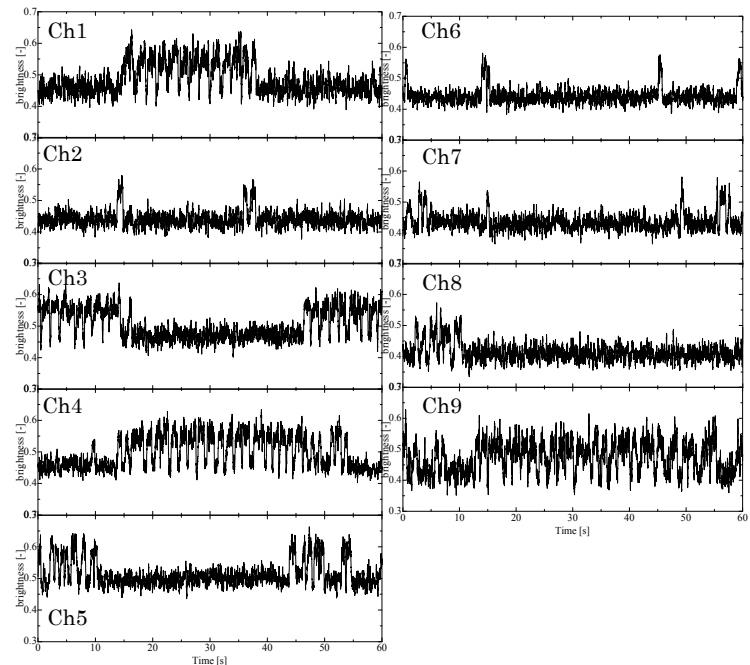
Fig.3   Image processing results in each channel.
(x_{ex}=0.1- G=50kg/m²s)

REFERENCES:
[1] H. Umekawa et al., The 25th National Symposium on Power and Energy Systems (2021) B135.
[2] R.Funakura et al., Thermal Engineering Conference (2021) B123.
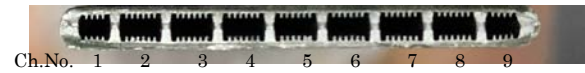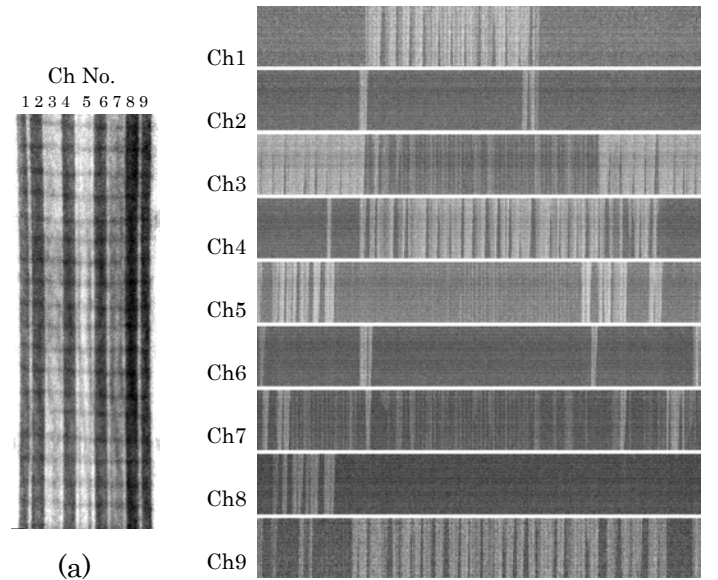[3] Sakai Master Thesis, Kansai Univ. (2021).

R3P5-4

Measurement of Frost Distribution by Using X-ray and Neutron Cooperative Imaging

R. Matsumoto[1], R. Kuroda[2], K. Kida[2], A. Fukai[2],
Y. Saito[3] D. Ito[3] and N. Odaira[3]

[1]*Faculty of Engineering Science, Kansai University*
[2]*Graduate School of Science and Engineering, Kansai University*
[3]*Institute for Integrated Radiation and Nuclear Science, Kyoto University*

INTRODUCTION: Recently, heat pumps have been proposed as an effective air conditioning system of heating operation for electric vehicles, because of the inability to use the engine heat as in the conventional vehicles. However, during the heating operation, frosting occurs on the outdoor heat exchanger of the air conditioning system. The frost formation causes a serious energy loss on the battery due to the heat transfer performance degradation by increasing the thermal resistance. In addition, the corrugated fin tube heat exchanger which is mainly used as an automotive heat exchanger has a more complicated structure than conventional one, hence it is difficult to capture the frosting situation. In this study, the frost deposition on the corrugated fin tube heat exchanger was evaluated by X-ray and neutron cooperative radiography imaging in a pseudo-three-dimensional measurement. Last year, the radiography images were obtained by the image intensifier. In this experiment, the scintillator is used for observing the detail frost distribution on the corrugated heat exchanger.

EXPERIMENTAL PROCEDURE: Figure 1 shows the schematic view of the experimental setup. The frost deposition between the fins is measured by irradiating X-ray parallel to the fins of the heat exchanger. The heat exchanger is made of aluminum. Thus, the frost deposition inside of the heat exchanger can be measured by irradiating neutron beam perpendicularly to the fins through the heat exchanger. Flow velocity of cooled humid air adjusted to at 1 m/sec is supplied to the test section. The test section consists of the styrofoam block duct with the corrugated fin tube heat exchanger. The heat exchanger was cooled by circulating the -21 ℃ fluorinert. The frost deposition on the heat exchanger was observed by CCD camera (Princeton Inst., 16-bit, 1024×1024 pixels and 512×512 pixels) with scintillator (Fujifilm Co., HR-Ultra Fast HR-16 and Chichibu Fuji Co., ZNSL-L100-AL1016) in every 10 sec for 1200 sec frosting duration. Exposure time is 8 sec for X-ray and 6 sec for neutron beam.

RESULTS: Figure 2 shows the front view of the corrugated fin tube heat exchanger. The heat exchanger consists of flat tubes and the brazed corrugated louver fins. The coolant flows in the parallel flat tubes and the humid air flows in the small fin channels formed by the corrugated louver fins. Figure 3 shows the frost deposition distributions on the heat exchanger using by the scintillator or the image intensifier. X-ray images show the frost formation observed from the front view of the heat exchanger. Last year, the frost deposition was overestimated by using image intensifier on the X-ray imaging. The detailed frost-deposition distribution can be measured by using the scintillator. clearly**.** The neutron images show the frost deposition inside of the heat exchanger. The main flow direction is left to right on the neutron images in Fig. 3. At 1200 sec, the frost deposits on the

fin front edge. Frost deposition decreases along the flow direction. There is no frost deposition in the downstream of area of the heat exchanger. This result shows the frost deposition distribution in the corrugated fin heat exchanger more clearly by X-ray and neutron cooperative imaging.
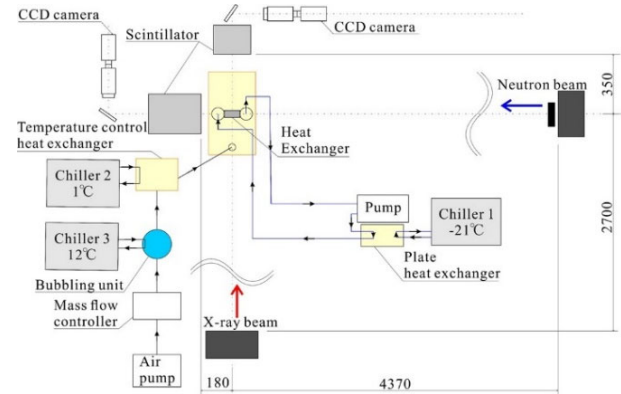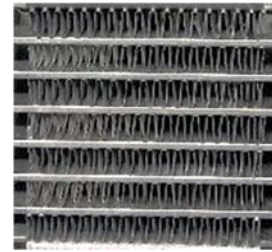

Fig. 1 Schematic view of the experimental setup.

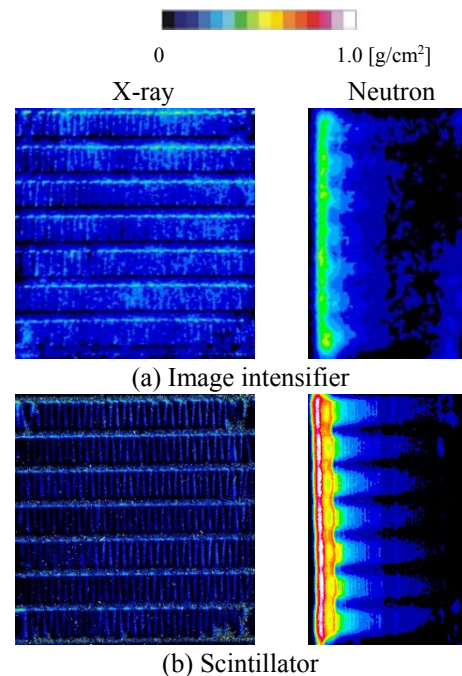
Fig. 2 Front view of the corrugated fin heat exchanger.

(a) Image intensifier

(b) Scintillator

Fig. 3 Frost deposition distributions observed by X-ray and neutron radiography at 1200 sec.

PR5-6 Introduction of contrast agent for X-ray-based visualization of roots planted on organic medium

Uzuki Matsushima[1], Daisuke Ito[2],
Yasushi Saito[2]

[1] *Faculty of Agriculture, Iwate University*
[2] *Institute for Integrated Radiation and Nuclear Science, Kyoto University*

INTRODUCTION: Rice husks are considered an industrial waste product and have been used in rice husk medium, which is a mixture of rice husks and soil at a 3:1 ratio by volume. This inexpensive medium has the advantage of being lightweight, easy to carry, and offers good drainage and resistance to plant root rot. Even if the bottom portion of a potted plant filled with rice husk medium were flooded with water, the capillary rise of the water was less than 8 cm. Therefore, the medium remained dry 8 cm above the waterlogged surface. We investigated the phenomenon of water movement by roots into the arid zone formed in the rice husk medium. This arid region is believed to be a key factor in the development of the plant's ability to tolerate salt. Neutron imaging is sensitive to water, but not minerals, making it suitable for studying water transfer from the soil to the roots. However, in media with high organic matter, such as the rice husk medium, it is difficult to distinguish between roots and the medium, which leads to inconclusive images. X-ray imaging is not suitable for plant root visualization because of its low sensitivity for biological samples. However, by introducing a contrast agent into the plant roots and increasing the absorption of X-rays compared to rice husk medium, roots in the rice husk medium could be observed. Therefore, this study established a method to locate roots in culture medium with high organic matter using X-ray imaging.

MATERIALS and METHODS: Common beans (*Phaseolus vulgaris* L.) were sown in aluminum containers (200 mm height, 25 mm width, and 25 mm depth) filled with rice husk medium and grown until the first true leaf developed. The shoot was cut off leaving approximately 20 mm from the root tip to introduce the iodine solution. To dehydrate the rice husk medium, the bottom of the aluminum container was opened to allow water to evaporate from the roots and nearby medium(Fig. 1). Three iodine solution concentrations of 0.10, 0.25 and 0.05 mol/L were used as treatments, and water was used as a control. The aluminum container was inverted to immerse the stem cut ends into the beaker containing the iodine solution, as shown in Fig. 1. After the cut ends of the sample stems were immersed in the contrast media for 24 hours, they were each packed in a plastic bag and shipped to KURNS, Kyoto University. X-ray imaging was performed at the B4 experimental chamber of the Kyoto University Reactor.
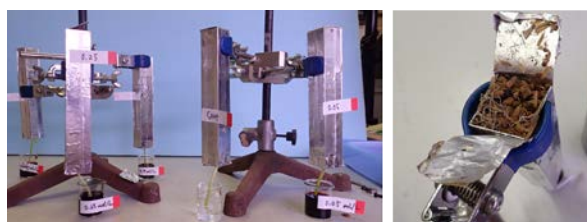

Fig. 1. Introduction of iodine solution into the sample. Left: at the time of introduction; Right: the bottom of the aluminum container is opened.
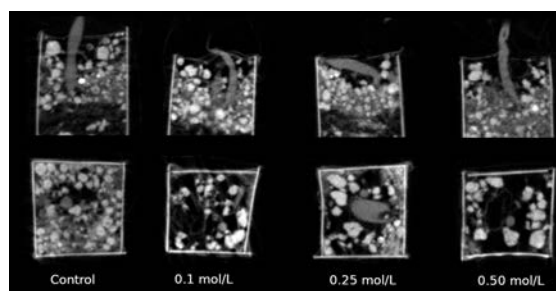

Fig. 2. X-ray CT image. The upper panel is a longitudinal section, and the lower panel is a transverse section. The brighter the pixel, the higher the X-ray absorption at that location.

RESULTS: The stems of the common bean plants turned brown all the way to the root tips after immersion in the iodine solution, confirming that the iodine solution had been introduced into the visible stem and root before the X-ray images were taken. In this experiment, the bottom of the aluminum container was opened to expose the medium and sample roots to air. This exposure caused the water potential of the roots to decrease due to the water vapor pressure difference between the sample root system and the surrounding air. The change created a difference between the root water potential and the osmotic potential of the iodine solution, which was sufficient to introduce the iodine solution into the plant body. The degree of darkness in the X-ray computed tomography (CT) image increased with the degree of the material's absorption of X-rays. The images of the sample stems and roots containing various concentrations of iodine solution were slightly brighter than that of the control sample root (Fig.2). This indicated that the iodine solution in the plant roots was not sufficient to enhance the X-ray absorption. The contrast agent must contain elements with higher X-ray absorptivity than the iodine solution. The increased X-ray absorption of the plant roots approached that of the soil in the rice husk medium, which made it difficult to distinguish between the roots and the soil in the image. For future studies, it will be necessary to track the visualized roots to determine their shape.

PR5-7   Effect of the water content of high-strength concrete on the spalling phenomenon under fire

M. Yoshioka, T. Hosokawa, A. You, A. Yasue, K. Kobayashi, J. Kim, M. Kanematsu, Y. Nishio[1], N. Odira[2], D. Ito[2] and Y. Saito[2]

Graduate School of Science and Technology, Department of Architecture, Tokyo University of Science
[1]Graduate School of Engineering, Department of Architecture, The University of Tokyo
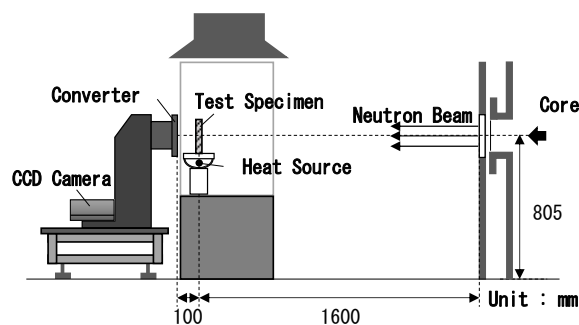*[2]Institute for Integrated Radiation and Nuclear Science, Kyoto University*

INTRODUCTION: In general, reinforced concrete buildings are fireproof structures because they have cover concrete to resist heat from a fire. However, spalling [1] phenomena may occur to lose their cover concrete when the structures were heated by fire, especially in case of using high strength concrete. In the past research, the explanations for this phenomenon have been widely accepted by thermal stress and water vapor pressure, or both. On the other hand, it has been pointed out that the spalling does not occur at the low water content but at the high moisture content. In this study, the effect of moisture content on the spalling phenomena of high-strength concrete was investigated by using the neutron imaging technique.

EXPERIMENTS: Heating experiments were performed on test specimens with target relative moisture contents of 20%, 40%, 60%, 80%, and 100%, in the KUR-B4 port of KURNS. Transmission images were obtained using neutron radiography to detect the moisture behavior inside the specimens to determine the moisture behavior inside the concrete. And at the same time, temperatures at 10 mm and 20 mm from the heating surface were measured by thermocouples. Fig.1 shows the schematic diagram of the test equipment used in the experiment. The specimens are 100×70×30 mm (width × height × thickness) of reinforcing rebar with a cover depth of 30mm. For comparison, two types of cement, Ordinary Portland Cement (OPC) and High-early Strength Cement (HSC), were used. The compressive strength of concrete measured on the day (18 days after the mixing) of the heating experiments was 153N/mm^2.

RESULTS: It observed the different trends in the spalling phenomenon by the hydrous condition between the specimens of OPC and HSC.
 Fig.2 shows an example of a change in the amount of moisture content inside the concrete. Fig.3. shows the relative moisture content inside the concrete just before the explosion. The moisture contents in the specimens tend to increase as the distance from the heating surface increases, regardless of the type of cement or the moisture content. On the other hand, the increase in the moisture content was

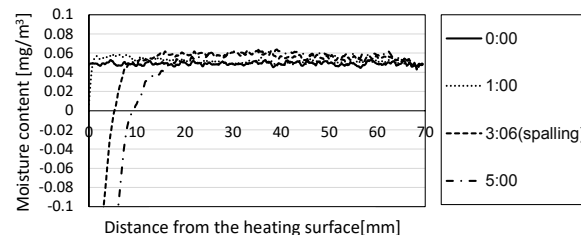Fig. 1 Schematic diagram of the heating experiment.

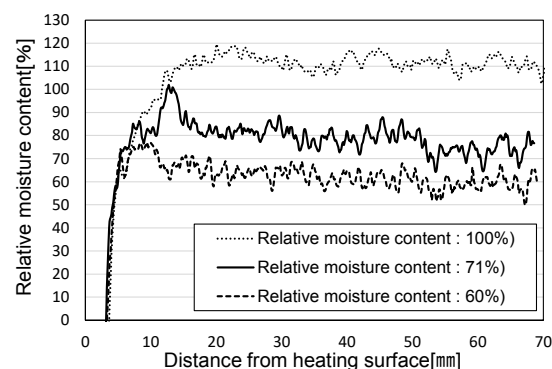Fig. 2 Changes in the amount of moisture content.

Fig. 3 The effect of initial relative moisture content on the relative moisture distribution just before the spalling.

only at most 0.02mg/mm^3, which is equivalent to about 30% of the initial relative moisture content. In addition, in this experiment, no localized increase in moisture content reported as "moisture clog" in previous studies was observed in the relative moisture distribution just before the spalling observed.
Cracks, which were thought to be due to the restraint of reinforcing bars during heating, were observed, however, the effect on the spalling phenomenon due to the presence or absence of reinforcing bars was not confirmed.
Considering the timing of spalling and cracking at the position of the reinforcing bar, it can be said that no cracks were observed in the specimens where thermal stresses were released by the spalling, suggesting that thermal stress may have contributed to the spalling phenomenon.

REFERENCES:
[1] JCI, (2017). "Committee Reports: JCI-TC-154A

R3P5-7

PR5-8   Visualization of Lithium Ion Migration in the Solid Electrolyte by Neutron Radiography

S. Takai[1], F. Song[1], H. Chen[1], K. Ota[1], T. Yamamoto[1], T. Yabutsuka[1], T. Yao[2], D. Saito[3], Y. Saito[3]

[1]*Graduate School of Energy Science, Kyoto University*
[2]*Kyoto University*
[3]*Institute for Integrated Radiation and Nuclear Science, Kyoto University*

INTRODUCTION: Enhancement of lithium ion conduction in oxide-based solid electrolyte is one of the focused issues for the development of All Solid-State Batteries. We have revealed that $LaPO_4$ dielectric particle dispersion in NASICON-type solid electrolyte LATP ($Li_{1.3}Al_{0.3}Ti_{1.7}(PO_4)_3$) improves the conductivity by 3 times [1-3]. The conductivity enhancement is thought to be due to the formation of space charge layer in the vicinity of $LaPO_4$ / solid electrolyte interface, in which the defect concentration is higher and thus the lithium diffusion occur faster [4]. We have recently measured the tracer diffusion coefficient of lithium ion in pristine and $LaPO_4$ dispersed LATP by means of neutron radiography [5]. Due to large neutron attenuation factor of ^6Li, diffusion profile has been obtained for LATPs consisting of ^7Li using ^6Li as the tracer.

In above experiments, diffusion process has been achieved by simply annealing after applying the tracer. On the other hand, in terms of the battery application, visualization of lithium migration in the solid electrolyte is also significant. In the last year, we have constructed MnO_2 / ^7Li-LATP / ^NLi-LATP / $Li_{1.33}Ti_{1.67}O_4$ cells to electrolyze for the neutron imaging. Herein, ^NLi indicates the natural isotope ratio of ^6Li / ^7Li. However, the lithium transfer at the interface is relatively difficult to observe the lithium migration in ^7Li-LATP. Then, in the present study, we changed the cell configuration as $LiMn_2O_4$ / ^7Li-LATP / $LiMn_2O_4$ symmetry cell to reduce the solid-solid interface.

EXPERIMENTS: ^7Li-LATP ($Li_{1.3}Al_{0.3}Ti_{1.7}(PO_4)_3$) and ^NLi-$LiMn_2O_4$ pellets were prepared by high-temperature solid-state reaction method. The surfaces of the samples were polished at the both sides of surface to ensure the flat plane with mirror finish. These samples were stacked as the illustration of Fig. 1, heated up to 300 °C to facilitate the lithium migration across the interface, and subjected 0.25 µA of DC current to lead the solid-state electrolysis. The photograph of the apparatus is also shown in Fig. 1. After the electrolysis was started, the entire apparatus was subjected to direct neutron beam for 45 minutes at B4 port of KUR (generated at 1MW). Neutron radiography images were taken by the CCD camera (5 min exposure) every 15 minutes.

RESULTS: Fig. 2 shows the typical radiography images of the symmetrical cell. Since the natural isotope abundance was employed for $LiMn_2O_4$, the image shows

darker in comparison with LATP. On the other hand, LATP shows the whiter image. Comparing the two images of $LiMn_2O_4$ / ^7Li-LATP / $LiMn_2O_4$ symmetry cell, no significant change was observed for LATP region, and the trace of lithium migration toward ^7Li-LATP cannot be detected. This would be due to the solid – solid interface between $LiMn_2O_4$ and LATP is rather severe, restricting DC current down to 1 µA. We are planning to paste $LiMn_2O_4$ slurry to resolve the difficulty in lithium migration across the interface.
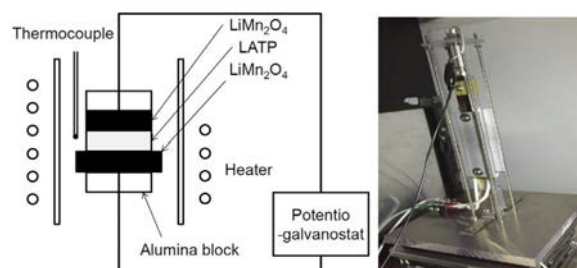

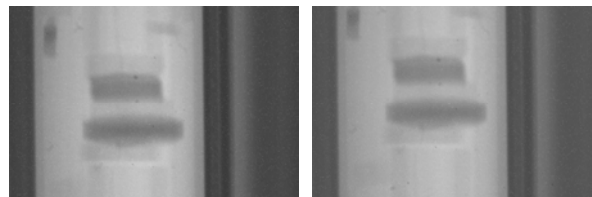Figure 1 Schematic view and photograph of the apparatus.

Figure 2 Radiography images of $LiMn_2O_4$ / ^7Li-LATP / $LiMn_2O_4$ symmetry cell after electrolyzed for (left) 1 h and (right) 3 h.

REFERENCES:
[1] H. Onishi *et al. Electrochemistry*. 84 (2016) 967.
[2] F. Song *et al. J. Alloys Compds*. 853(2021)157089.
[3] F. Song *et al.*, *Materials* 14 (2021) 3502.
[4] C. C Liang. *J. Electrochemical Soc*. 120 (1973) 1289.
[5] F. Song *et al.*, *Solid State Ionics* 377 (2022) 115873.

R3P5-11

PR5-9   Visualization in the Accumulated Curved Rod Arrays

M. Kaneda, Z. Li, M. Sugimoto

Department of Mechanical Engineering, Osaka Prefecture University

INTRODUCTION: Electrification of vehicles has been promoted to reduce greenhouse gas. The powertrain of the vehicles is the electric motors which is required to have high performance, more power, and compactness [1]. This leads to the higher emission heat density from the motor package and the effective cooling scheme of the heated stator coil has been important. The stator coil in the motor is cooled by the coolant poured from a nozzle above. Although there have been some studies of the temperature measurement [2, 3], the coolant profile inside the coil has not been clarified yet and the pouring conditions are decided empirically. In this study, therefore, the coolant visualization inside the simplified stator coil structure is carried out by using the neutron radiography. The coil structure is made of aluminum and composed by layered curved rod array.

EXPERIMENTS: The schematic model of the experiment is shown in Fig.1(a). The stator coil is presumed by the accumulated curved rod arrays shown in Fig.1(b) where the coolant is directly poured from above. Each square rod is made of aluminum and aligned with a gap of 1mm. This roughly corresponds to the enlarged stator coil structure.

The flow rate of the coolant is 0.5-0.65L/min and the temperature of the coolant is varied from 20-50 degree C. The neutron beam is in horizontal and coaxial direction to the curved coil structure.
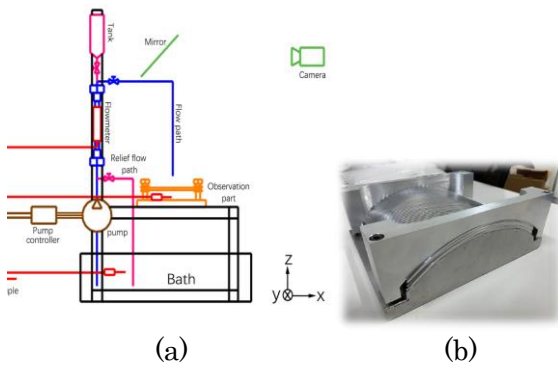

(a)   (b)

Figure 1. Experimental setup. (a) schematics (b) enlarged stator coil structure

RESULTS: The visualized image of one condition is shown in Fig. 2(a). As expected, the fluid spreads along the structure at lower layer. The rest of the fluid goes down vertically. This profile is converted to the cylindrical coordinate to investigate the fluid volume inside the structure as shown in Fig. 2(b). The fluid profile depends on the flow rate and temperature. Since the fluid viscosity decreases at higher temperature, the fluid area decreases. The higher the flow rate results in the large fluid area.

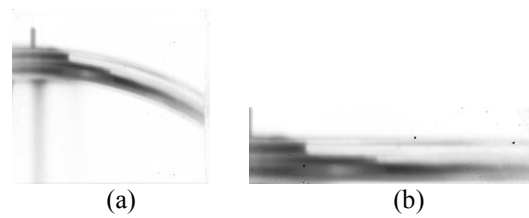(a)   (b)

Figure 2. Visualized coolant profile. (a) snapshot (b) converted to cylindrical coordinate.

By using the neutron attenuation factor of the fluid, the local fluid volume in the spanwise direction can be estimated, which is shown in Figure 3 at 500mL/min. This supports the quantitative temperature dependence.
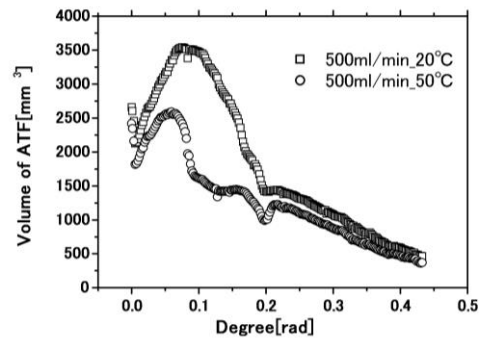

Figure 3. Volume profile of the fluid at 0.5L/min along the circular direction.

The total fluid volume in the structure can be calculated by the integration of the local profile. The flow rate and the temperature dependency can be regarded as the dimensionless number in the horizontal axis and the volume can be normalized by the nozzle diameter, which is partially shown in Figure 4. This yields the linear correlation successfully.
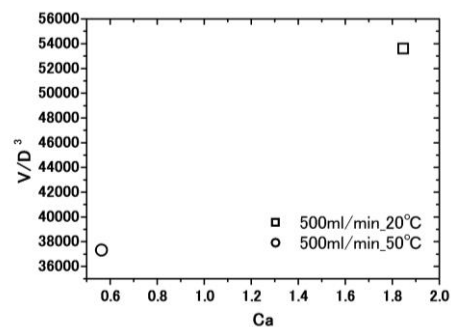

Figure 4. Dimensionless volume versus Capillary number at 0.5L/min.

REFERENCES:
[1] N. Kobayashi and T. Ikegami, Thermal Sci. Eng., **15**, 2 (2007) 49-54.
[2] T. Davin *et al*., Applied Thermal Eng., **75** (2015) 1-13.
[3] S. Onimaru e*t al*., Denso Technical Review, **13** (2008) 19-25.

R3P5-12